JBC RESEARCH ARTICLE

Paraspeckle subnuclear bodies depend on dynamic heterodimerisation of DBHS RNA-binding proteins *via* their structured domains

Received for publication, April 7, 2022, and in revised form, September 23, 2022 Published, Papers in Press, October 7, 2022,
https://doi.org/10.1016/j.jbc.2022.102563

Pei Wen Lee[1,2], Andrew C. Marshall[3], Gavin J. Knott[3], Simon Kobelke[1,2], Luciano Martelotto[1,2], Ellie Cho[4,5], Paul J. McMillan[6], Mihwa Lee[7], Charles S. Bond[3], and Archa H. Fox[1,2,3,*]

From the [1]The School of Human Sciences, [2]The Harry Perkins Institute of Medical Research, QEII Medical Centre, Nedlands, and The Centre for Medical Research, and [3]School of Molecular Sciences, The University of Western Australia, Crawley, WA, Australia; [4]Department of Biochemistry & Molecular Biology, and [5]The Biological Optical Microscopy Platform, The University of Melbourne, Melbourne, VIC, Australia; [6]Centre for Advanced Histology & Microscopy, Peter MacCallum Cancer Centre, Melbourne, VIC, Australia; [7]Department of Biochemistry and Genetics, LaTrobe University, Bundoora, VIC, Australia

Edited by Ursula Jakob

RNA-binding proteins of the DBHS (*Drosophila* Behavior Human Splicing) family, NONO, SFPQ, and PSPC1 have numerous roles in genome stability and transcriptional and posttranscriptional regulation. Critical to DBHS activity is their recruitment to distinct subnuclear locations, for example, paraspeckle condensates, where DBHS proteins bind to the long noncoding RNA NEAT1 in the first essential step in paraspeckle formation. To carry out their diverse roles, DBHS proteins form homodimers and heterodimers, but how this dimerization influences DBHS localization and function is unknown. Here, we present an inducible GFP-NONO stable cell line and use it for live-cell 3D-structured illumination microscopy, revealing paraspeckles with dynamic, twisted elongated structures. Using siRNA knockdowns, we show these labeled paraspeckles consist of GFP-NONO/endogenous SFPQ dimers and that GFP-NONO localization to paraspeckles depends on endogenous SFPQ. Using purified proteins, we confirm that partner swapping between NONO and SFPQ occurs readily *in vitro*. Crystallographic analysis of the NONO-SFPQ heterodimer reveals conformational differences to the other DBHS dimer structures, which may contribute to partner preference, RNA specificity, and subnuclear localization. Thus overall, our study suggests heterodimer partner availability is crucial for NONO subnuclear distribution and helps explain the complexity of both DBHS protein and paraspeckle dynamics through imaging and structural approaches.

NONO (Non-POU domain-containing octamer-binding protein), SFPQ (splicing factor proline and glutamine rich), and PSPC1 (paraspeckle component protein 1) comprise the three proteins of the DBHS (*Drosophila* behavior human splicing) protein family in complex vertebrates. NONO, SFPQ, and PSPC1 share 50% sequence identity and typically exist as dimers (1–3) (Fig. 1). The core conserved region of DBHS proteins is composed of tandem RNA recognition motif (RRM) domains, a NOPS (NONA/ParaSpeckle) domain (an Interpro defined domain that is only found in this protein family), and an extended coiled-coil and is responsible for dimerization and interaction with RNA (4). 3D atomic structures of this core region have revealed an extensive dimer interface between monomers, supporting the notion that these proteins are obligate dimers (3, 5–7). In HeLa cells, the majority of DBHS proteins are NONO-SFPQ heterodimers, with a smaller pool of NONO-PSPC1 heterodimers (2). However, little is known about the structural and dynamic constraints of different partner choice for DBHS heterodimers and the subsequent functional roles of different DBHS dimers.

DBHS proteins are implicated in numerous aspects of gene regulation and expression, such as transcriptional regulation, splicing regulation, RNA transport, pri-miRNA processing, miRNA targeting, and DNA repair, with these functions correlated with their presence at different subnuclear and subcellular locations (reviewed in (4)). One such example of DBHS function in the nucleus is their essential role in the formation of subnuclear bodies termed paraspeckles (8). The structural backbone of paraspeckles is a long noncoding RNA, named NEAT1 (Nuclear Paraspeckle Assembly Transcript 1) (9–11). Upon NEAT1 transcription, DBHS proteins bind the RNA, extensively coating it through oligomerization, conferring increased stability to the RNA and forming a ribonucleoprotein (RNP) particle (6, 12). Approximately, 50 NEAT1-DBHS RNPs are then arranged into a single mature paraspeckle *via* liquid-liquid phase separation (LLPS) mediated by the low complexity region of the accessory protein FUS, as well as recruitment of over 40 additional RNA-binding proteins to the paraspeckle (13, 14). Paraspeckles are found in various mammalian cultured cells and tissues, including primary and transformed cell lines (8, 15, 16), with the exception

* For correspondence: Archa H. Fox, Archa.fox@uwa.edu.au.
Present address for Luciano Martelotto: Adelaide Centre of Epigenetics, South Australia ImmunoGENomics Cancer Institute, The University of Adelaide, 5005, South Australia, Australia.
Present address for Pei Wen Lee: Institute of Medical Biology, Agency for Science, Technology, and Research, Singapore 138,648.
Present address for Gavin J. Knott: Department of Biochemistry, Monash University, Clayton Victoria, Australia.

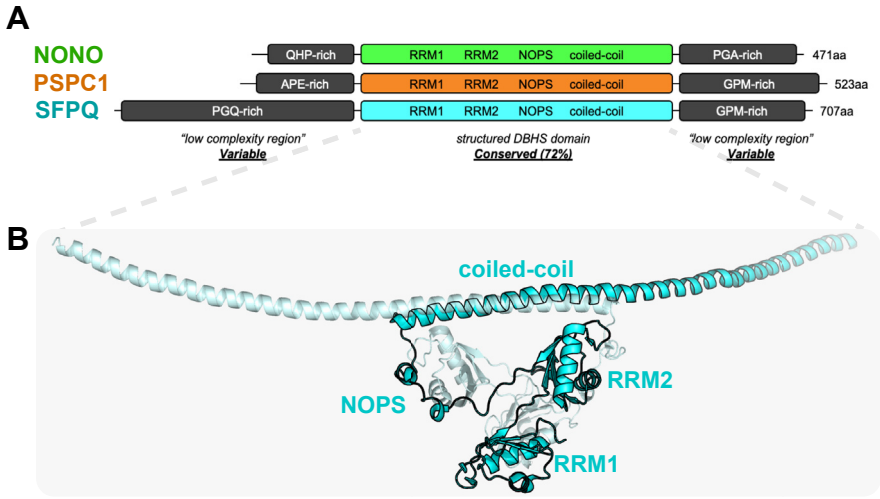

Figure 1. DBHS protein family members form homodimers and heterodimers dimers. Each member contains a core conserved region flanked by variable regions of low sequence complexity. *A*, schematic alignment of the three human DBHS proteins, SFPQ, NONO, and PSPC1, with relevant domain detail highlighted. *B*, X-ray crystal structure showing the dimer formed by the conserved DBHS region (SFPQ homodimer; PDB 4wij; residues 276–598). The domains of one dimer partner (*black outline*) are labeled. PDB, Protein Data Bank.

of embryonic stem cells (11). Organization of proteins into paraspeckles can enhance the efficiency of paraspeckle protein functions in pri-miRNA RNA processing (17). A variety of cellular stresses, including hypoxia and viral infection, lead to an increase in paraspeckle size and abundance, and this paraspeckle induction correlates with cancer progression of some cancer types (18).

Recently paraspeckles were mapped at the ultrastructural level in fixed cells using super-resolution structured illumination microscopy (SIM), revealing an unusual core-shell molecular organization (14). FISH against different parts of NEAT1, combined with immunofluorescence against paraspeckle proteins revealed the central part of the 23 kb NEAT1 RNA is found in the core of the paraspeckle, along with SFPQ, NONO, PSPC1, and FUS. In contrast, the 5′ and 3′ ends of NEAT1 and TARDBP proteins are found in the shell of the paraspeckle. Several other proteins (RBM14 and BRG1) bridge the two zones. Paraspeckles can either be single, approximately spherical units of 360 nm diameter, or chains of paraspeckle units, with a constant 360 nm width and varying length, up to 2 microns (14, 19, 20). Given that paraspeckles are very dynamic structures, forming rapidly in response to stress and disassembling just as rapidly under different conditions (indeed in less than 30 min in some cases (21)), it is important to complement these fixed cell super resolution observations with live cell studies.

In this study, we have used cellular paraspeckle imaging experiments and *in vitro* methods to characterize DBHS protein dimers. We generated a HeLa stable cell line with inducible GFP-NONO to examine its targeting to paraspeckles and perform live cell 3D-SIM imaging of NONO-labeled paraspeckles, revealing how they twist and form in real time. We show that NEAT1 and SFPQ are both involved in targeting NONO to paraspeckles, but to different extents, revealing a critical role for SFPQ in targeting the NONO-SFPQ heterodimer to distinct nuclear locations. Given the key role of the NONO-SFPQ heterodimer, we also perform *in vitro* studies to show rapid partner swapping of NONO and SFPQ homodimers, with a preference for the heterodimer state. Finally, we describe the NONO-SFPQ crystal structure and how key differences could explain the heterodimerization preference.

Results

Generation and characterization of a HeLa$^{GFP\text{-}NONO}$ stable cell line

Of the three DBHS proteins, PSPC1, was named Paraspeckle Protein Component 1, as it was the first paraspeckle marker protein and it has been extensively used in prior live cell paraspeckle studies (8). However, as PSPC1 is in fact dispensable for paraspeckle formation, we generated a tool for live cell imaging of paraspeckles with fluorescently tagged NONO, an essential paraspeckle protein component. We therefore generated a HeLa$^{GFP\text{-}NONO}$ stable cell line that constitutively expresses the Tet-On 3G transactivator and contains a genomically integrated P_{TRE3G}–tagGFP–NONO plasmid (hereafter termed GFP-NONO) that expresses GFP-NONO only in the presence of Doxycycline (Dox, Fig. 2*A*). Dox concentrations above 25 ng/ml induced an appropriately low level of exogenous GFP-NONO that was consistently less abundant than that of the endogenous NONO (Fig. 2*B*). Furthermore, the expression level of endogenous NONO was unaffected by the small and stable expression of GFP-NONO (Fig. 2*B*). As a result, we used 50 ng/ml Dox for the remainder of the study. Of note, extending the duration of Dox treatment to 48 h did not result in excess GFP-NONO nor adverse autoregulatory effects on endogenous NONO levels (Fig. 2*C*). To observe the stability of GFP-NONO, we induced expression for 24 h, then analyzed NONO levels over the

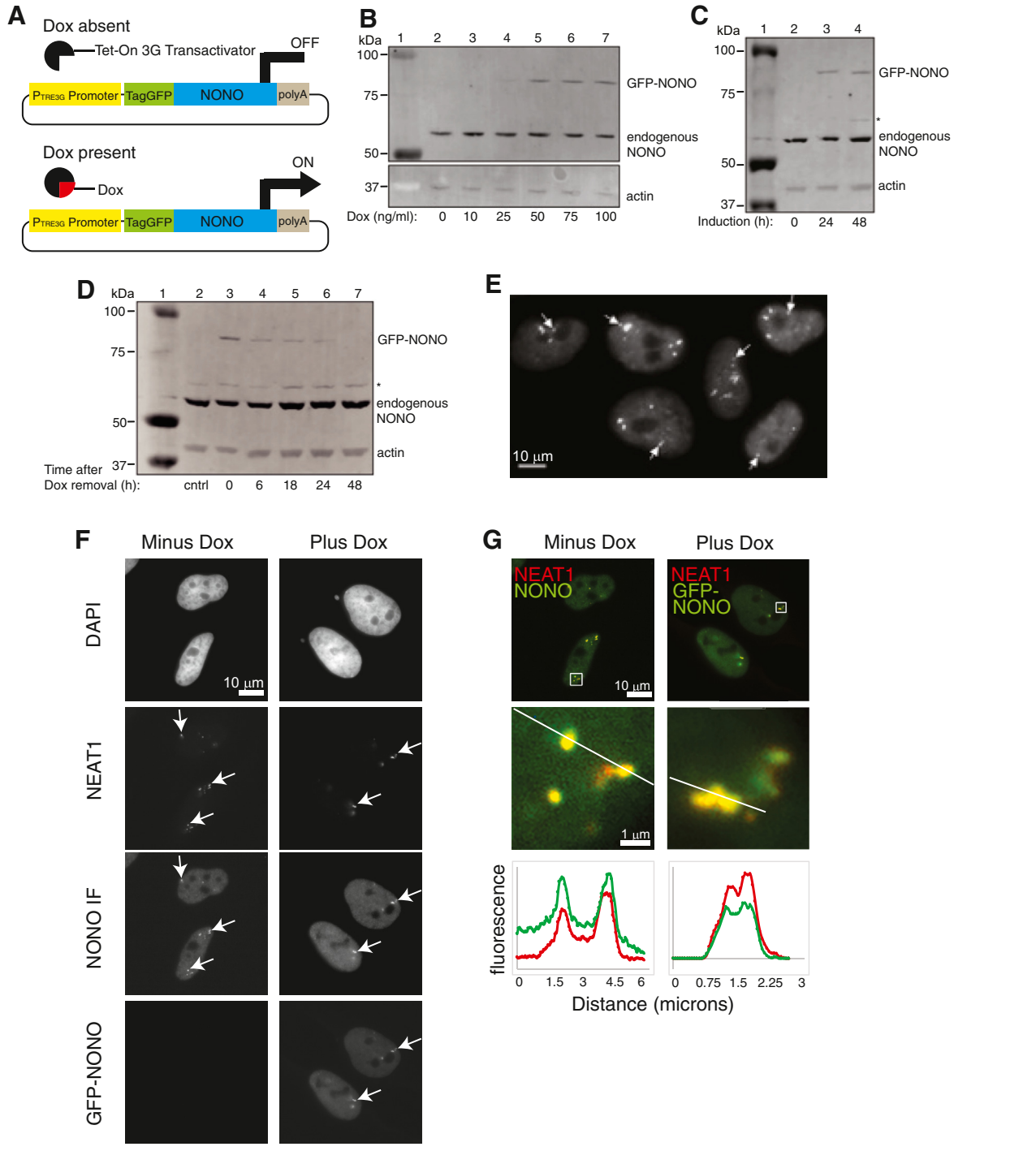

Figure 2. Generation and characterization of a stable HeLa$^{GFP\text{-}NONO}$ cell line. *A*, schematic representation of a P_{TRE3G}–tagGFP–NONO plasmid that was transfected in HeLa cells constitutively expressing the Tet-On 3G transactivator to generate a stable HeLa$^{GFP\text{-}NONO}$ cell line. Expression of GFP-NONO is induced only in the presence of Dox. *B*, Western blot of protein lysates extracted from HeLa$^{GFP\text{-}NONO}$ cells that have been induced with a range of concentrations of Dox for 24 h, showing that different concentrations of Dox gave different levels of expression of GFP-NONO but endogenous NONO remained constant. Molecular weight markers (kDa) are at left. Anti-NONO monoclonal antibody was used to probe for GFP-NONO (82 kDa) and endogenous NONO (55 kDa). Beta Actin (45 kDa) was used as the loading control. *C*, Western blot of protein lysates extracted from HeLa$^{GFP\text{-}NONO}$ cells that have been induced with 50 ng/ml of Dox over different times. Induction with Dox for both 24 h and 48 h gave similar expression level of GFP-NONO. Proteins were detected as in (*B*). *denotes some sporadic cross-reactivity of the NONO antibody with endogenous PSPC1. *D*, Western blot of protein lysates extracted from HeLa$^{GFP\text{-}NONO}$ cells that have been induced with 50 ng/ml of Dox for 24 h, followed by removal of Dox for different times ranging from 0 to 48 h. Upon withdrawal of Dox, detectable amount of GFP-NONO gradually decreased over time. Proteins were detected as in (*B*). Sample not induced with Dox serves as negative control in lane 1. *denotes some sporadic cross-reactivity of the NONO antibody with endogenous PSPC1. Panels (*B–D*) are single representative blots from multiple repeated experiments (minimum n = 3). *E*, widefield fluorescent micrograph of several fixed HeLa$^{GFP\text{-}NONO}$ cells showing bright and distinct paraspeckles, *arrows*, with nucleoplasmic background signal. *F*, representative fluorescence micrographs of HeLa$^{GFP\text{-}NONO}$ cells either without Dox induction (*left*) or following Dox induction (*right*) show that GFP-NONO localizes with NEAT1 in paraspeckles in an identical manner to endogenous NONO. Top to bottom: DAPI; NEAT1 FISH to detect paraspeckles; anti-NONO immunofluorescence to detect endogenous NONO (*left*) and a mixture of endogenous NONO and Dox-induced GFP-NONO (*right*); and GFP-NONO fluorescence. *Arrows* indicate colocalization in paraspeckles. The scale bar represents 10 µm. *G*, merged fluorescence images of selected channels from (*F*), showing at *left* that in the

following 48 h, observing a detectable amount of GFP-NONO 24 h after Dox removal but not after 48 h (Fig. 2*D*).

We next verified that the induced GFP-NONO was appropriate for use as a clear marker for paraspeckles. Fixed and induced HeLa$^{GFP\text{-}NONO}$ cells displayed bright and distinct subnuclear puncta, as marked by the green fluorescence of GFP-NONO (Fig. 2*E*, arrows). The identity of paraspeckles was confirmed by colocalization of endogenous NONO (Fig. 2, *F* and *G*, left panels) with FISH against the long noncoding RNA, NEAT1 (Fig. 2, *F* and *G*, arrows show paraspeckles, Fig. S2 shows additional representative images). We next tested if the Dox-induced GFP-NONO displayed similar behavior to endogenous NONO with respect to colocalization with NEAT1 in paraspeckles. Figure 2, *F* and *G*, right panels show that, indeed, as with endogenous NONO, the low levels of Dox-induced GFP-NONO also colocalize with NEAT1 in an identical manner. Line scans through individual paraspeckles confirm no change in localization behavior between endogenous NONO (Fig. 2*G*, green, left) and GFP-NONO (Fig. 2*G*, green, right) with respect to paraspeckles/NEAT1 colocalization (Fig. 2*G*, red). 3D-SIM imaging of the samples also showed clear colocation of GFP-NONO and NEAT1 (volume view in Fig. S1). Taken together, the generated HeLa$^{GFP\text{-}NONO}$ cells were confirmed as an appropriate tool for studying paraspeckles in living cells, as they express low levels of exogenous GFP-NONO marking paraspeckles, as defined by colocalization with NEAT1.

Nascent GFP-NONO localizes to paraspeckles

Given the many roles and nuclear locations of DBHS proteins, we sought to examine the temporal localization of GFP-NONO after its translation in the cytosol prior to its recruitment to paraspeckles. Live cell time-lapse fluorescence imaging of HeLa$^{GFP\text{-}NONO}$ cells was performed to observe localization changes of nascent GFP-NONO over a period of 24 h upon induction with Dox (Fig. 3*A*). Cells were counterstained with Hoechst 33342 nucleic acid dye to easily mark nuclei prior to the experiment. Images were taken every 30 min and fluorescence from GFP-NONO was first detected at the 12th hour of induction, followed by increasing fluorescence signal over time (Fig. 3, *A* and *B*, arrows show paraspeckles). The first detectable GFP-NONO fluorescence appears to be within paraspeckles, and with continued induction with Dox, the emerging fluorescently green nuclear foci persisted, enlarged, and increased in numbers over time. At the 18th hour of induction, bright and distinct paraspeckles were readily visible, hence indicating that 18 h of induction is sufficient for expressing the amount of GFP-NONO that can provide for clear observation of paraspeckle localization and behavior. Further induction till the 24th hour gave bright and distinct paraspeckles that are reminiscent of the ones obtained previously (Fig. 2, *E* and *F*). Thus, nascent GFP-NONO molecules directly accumulate at paraspeckles, without first transiting or becoming enriched in any other clearly discernible subcellular structure.

3D-SIM imaging of paraspeckles in living cells reveals growth characteristics

Since GFP-NONO has been proved to be a reliable marker for paraspeckles, it was of interest to observe the enlargement of paraspeckles over time. Proteasome inhibition *via* treatment with the drug MG132 can induce enlargement and elongation of paraspeckles (22). To observe any MG132-mediated changes in appearance of GFP-NONO–labeled paraspeckles over time, we performed time-lapse fluorescence imaging of Dox-induced HeLa$^{GFP\text{-}NONO}$ cells over a period of 12 h upon treatment with 1 μM of MG132 (Fig. 3*C*). Marked enlargement of paraspeckles was observed, although at this resolution, it was not possible to distinguish elongation from increased paraspeckle numbers (Fig. 3, *C* and *D*).

To gain deeper insights into the growth, elongation and formation of paraspeckles, we performed 3D-SIM time-lapse fluorescence imaging on MG132-treated cells over a period of 2 h, according to the timeline illustrated in Figure 4*A*. Due to the larger number of exposures required to reconstruct a 3D-SIM dataset, the number of images acquired was minimized to reduce phototoxicity and photobleaching.

This enhanced visualization of paraspeckles in 3D allowed us to see, for the first time, how paraspeckles can twist and grow over time. Figure 4*B* shows a representative MG132-treated cell captured over time with 3D-SIM. Unexpectedly, apparent MG132-mediated elongation of paraspeckles could not be observed in this instance, perhaps due to the short time course of imaging. However, several cells revealed the initial appearance of newly formed GFP-NONO–labeled paraspeckles followed by their gradual growth and enlargement through the rest of the live-imaging experiment (Fig. 4*B*, arrow shows newly formed paraspeckle). With 3D rendering as shown in Figure 4*C*, visualizations of newly formed paraspeckles (in *yellow*) and an adjacent existing paraspeckle (in *green*) were obtained. Imaging of additional live cells allowed the monitoring of changes in individual paraspeckles over the 2 h time course (Fig. S3). Overall, this imaging reveals the extent with which individual paraspeckles change shape and conformation in this short time frame. These studies reveal the dynamics of paraspeckle growth in line with their role as immediate stress responsive structures.

NONO localization in paraspeckles is dependent on NEAT1 and SFPQ

We next examined how the individual ablation of the key NONO-associated molecules, NEAT1, SFPQ, and PSPC1, using

absence of Dox, endogenous NONO (*green*) colocalizes with NEAT1 (*red*) in paraspeckles (*yellow*). *Right panel* shows in the presence of Dox, GFP-NONO (*green*) colocalizes with NEAT1(*red*) in paraspeckles (*yellow*). *Top panels* show overview, *middle panel* shows zoomed in paraspeckle clusters corresponding to *white boxes* in top panel. Bottom panel shows line-scan profile of the red and green fluorescence signals across the line as displayed in the *middle panel*. Western blots and micrographs are representative examples of >3 biological replicates. DAPI, 4′,6-diamidino-2-phenylindole; Dox, Doxycycline.

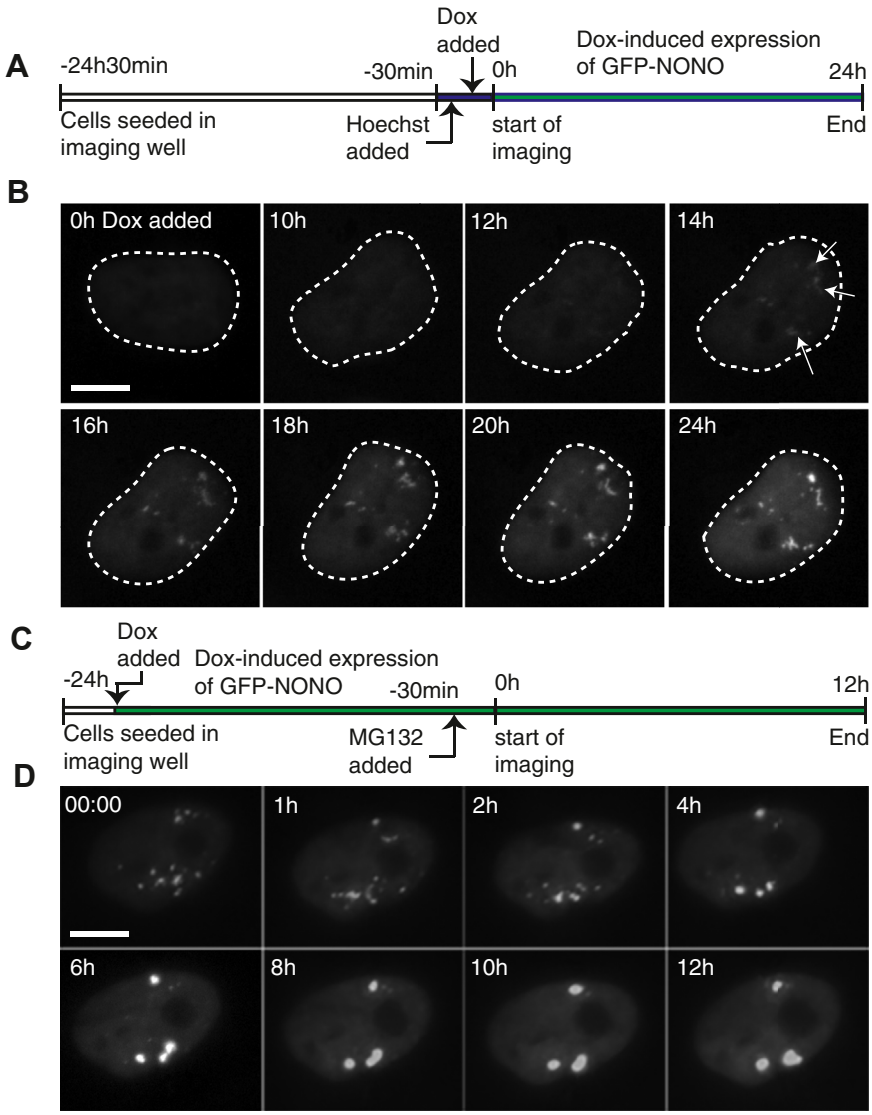

Figure 3. Early paraspeckle localization of newly imported GFP-NONO and increased GFP-NONO labeled paraspeckle abundance with proteosome inhibition. *A*, experimental timeline for live-cell observation of the 'birth' of newly made exogenous GFP-NONO when HeLa$^{GFP\text{-}NONO}$ cells were induced with 50 ng/ml Dox at the start of live imaging. Cells were preincubated with Hoechst 33342 for 30 min, to label DNA in *blue* prior to live imaging. *Blue* section represents DNA labeling with Hoechst 33342 dye; *green* section represents induction with Dox. *B*, fluorescent micrographs of a representative HeLa$^{GFP\text{-}NONO}$ cell acquired over the course of a 24 h live-cell imaging experiment, where images were taken every 30 min. Emerging green fluorescence displayed localization of nascent GFP-NONO to paraspeckles in the nuclei. These paraspeckles persist and gradually enlarge throughout the imaging experiment. The scale bar represents 10 μm. *Arrows*, paraspeckles. *C* and *D*, treatment with MG132 shows enlargement and growth of paraspeckles over time. *C*, experimental timeline for live-cell observation of the enlargement of GFP-NONO–labeled paraspeckles when induced with MG132 at the start of live imaging. *Green* section represents induction with Dox. *D*, fluorescence micrographs of a representative HeLa$^{GFP\text{-}NONO}$ cell acquired over the course of a 12 h live-cell imaging experiment upon treatment with MG132, where images were taken every 1 h. The scale bar represents 10 μm. Images are stills from representative movies, showing typical patterns as observed in many other cells (each being a technical replicate) imaged in the same experiment (minimum n = 10 cells). Dox, Doxycycline.

siRNAs, would alter the localization of GFP-NONO. To validate effective siRNA-mediated knockdown (KD) of SFPQ or PSPC1, Western Blotting was conducted, confirming markedly decreased expression of each protein in HeLa$^{GFP\text{-}NONO}$ cells treated with the respective siRNAs (Fig. 5*C*). Real-time quantitative PCR performed on HeLa$^{GFP\text{-}NONO}$ cells treated with NEAT1 siRNA showed more than 70% efficiency in knocking down NEAT1 (Fig. 5*D*). The siRNA-mediated resultant changes in GFP-NONO localization were examined *via* microscopy on fixed induced cells. In line with previously reported studies (10), cells treated with NEAT1 siRNA showed loss of paraspeckles as observed by NEAT1 FISH (Fig. 5*A*, central panel), although it should be noted that some residual NEAT1 foci were sometimes apparent in the NEAT1 siRNA-treated cells, but these foci were markedly reduced in size compared with control cells (Fig. 5*A*). When NEAT1 was knocked down, the background GFP-NONO fluorescence within the nucleus also increased relative to control cells (Fig. 5*A*), with a diffuse distribution of nuclear GFP-NONO. Thus, ablation of NEAT1 and paraspeckles by NEAT1 siRNA resulted in redistribution of GFP-NONO to the rest of the nucleoplasm.

It was previously shown that SFPQ KD results in reduced levels of NEAT1 RNA and the disassembly of paraspeckles (10). KD of SFPQ in the HeLa$^{GFP\text{-}NONO}$ cells indeed reduced

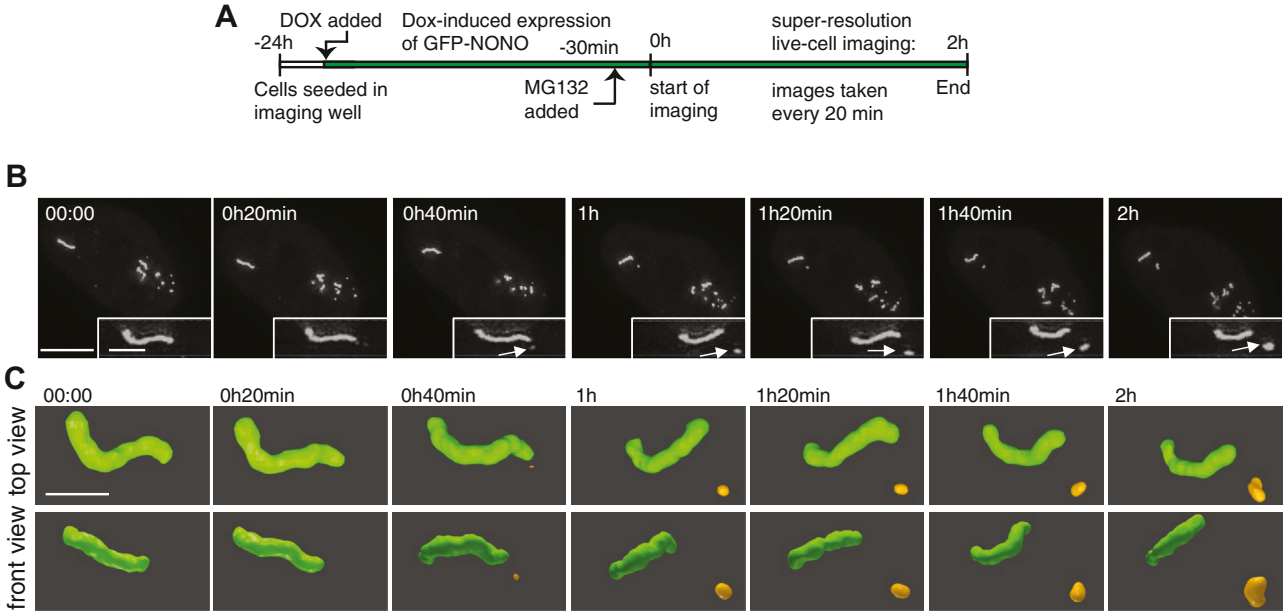

Figure 4. Super-resolution live imaging allows depiction of growth of paraspeckle over time. *A*, experimental timeline for super-resolution live-cell observation of the growth of GFP-NONO–labeled paraspeckles when induced with MG132, to encourage growth of paraspeckles, at the start of live imaging. *Green* section represents induction with Dox. *B*, super-resolution fluorescent micrographs of a representative HeLa$^{GFP\text{-}NONO}$ cell acquired over the course of a 2 h live-cell imaging experiment upon treatment with MG132, where images were taken every 20 min. The scale bar represents 5 μm. Inset shows paraspeckles at the *top left corner*, magnified to show dynamics of an existing paraspeckle, and the appearance and gradual growth of an adjacent newly formed paraspeckle. Arrows, growing paraspeckle. The Scale bar of inset represents 1 μm. *C*, Imaris/Blender 3D visualizations and rendering of 3D *top* orthogonal (*top row*) and front orthogonal (*bottom row*) views of magnified paraspeckles, showing enhanced visualizations of how individual paraspeckles twist, appear, and grow over time. The growing paraspeckle is marked in *yellow* at every time point. The scale bar represents 1 μm. Images are stills from one cell imaged in the experiment, with features of interest. The experiment was one biological replicate, with each movie of a single cell being a technical replicate. Dox, Doxycycline.

paraspeckles, as seen by diminished NEAT1 foci (Fig. 5*A* central panel). However, in the absence of both SFPQ and paraspeckles, GFP-NONO exhibited a distinctly different localization compared to paraspeckle reduction alone; in this case, numerous NONO-labeled nuclear aggregates were observed (Fig. 5*A*). The randomly assorted GFP-NONO foci are more numerous (Fig. 5*B*, upper plot) and smaller than the GFP-NONO paraspeckles observed in the scrambled control (Fig. 5*B*, lower plot). Finally, PSPC1 KD had little effect on GFP-NONO localization either inside or outside paraspeckles, as GFP-NONO localization was unchanged in the absence of PSPC1 (Fig. 5*A*).

NONO and SFPQ are dynamic heterodimers in vitro

Given the altered localization of NONO in the absence of SFPQ, but not PSPC1 (Fig. 5*A*), we wondered if this was indicative of dynamic switching of DBHS proteins into different dimer configurations that then influenced subnuclear localization. Of note, recombinant SFPQ and NONO core DBHS regions expressed in *Escherichia coli* purify as heterodimers *in vitro* (6), suggesting that a heterodimer of NONO-SFPQ is the more favored state over either homodimeric SFPQ or NONO. In agreement with this, analytical ultracentrifugation experiments show that the apparent dissociation constant of this NONO-SFPQ heterodimer is ∼3-fold lower than that of the SFPQ homodimer (7). To investigate this further, we purified homodimeric hexahistidine-tagged SFPQ (H_6SFPQ) and untagged homodimeric NONO to test for their ability to swap dimerization partner *in vitro* (Fig. 6). In nickel-affinity pull-down experiments, we observed that when 1:1 mixtures of the two homodimers were loaded onto a column, it was the heterodimer that eluted (Fig. 6*A*). We then characterized a complex of SFPQ and a maltose-binding protein fusion of NONO (MBP-NONO) using analytical size-exclusion chromatography (Fig. 6*B*). The complex of SFPQ and MBP-NONO elutes between the two homodimeric peaks, confirming that they are able to readily exchange partner to form a stable heterodimer. Thus, incubating SFPQ and NONO homodimers shows DBHS proteins rapidly exchange dimerization partner *in vitro*. Taken together, these data could be used to support the notion that the NONO-SFPQ heterodimer is the favored combination both *in vitro* and inside cells.

Crystal structure of SFPQ-NONO core dimerization region

While 3D atomic structures for the three human DBHS protein homodimers (Protein Data Bank [PDB] IDs 4wii, 5ifm, 5ifn) and two heterodimers, NONO-PSPC1 (3sde) and SFPQ-PSPC1 (5wpa), have been published previously (3, 6, 7, 23), the predominance of the NONO-SFPQ heterodimer in cells and its essential role in paraspeckle formation prompted us to determine its structure, completing the repertoire of structures for all six human DBHS dimer combinations. The X-ray crystal structure of a heterodimer containing the core DBHS region of SFPQ (residues 276–535) and NONO (residues 53–312) was determined by molecular replacement using data to 2.3 Å in space group $P3_121$ (7lrq; Table S1). The asymmetric unit

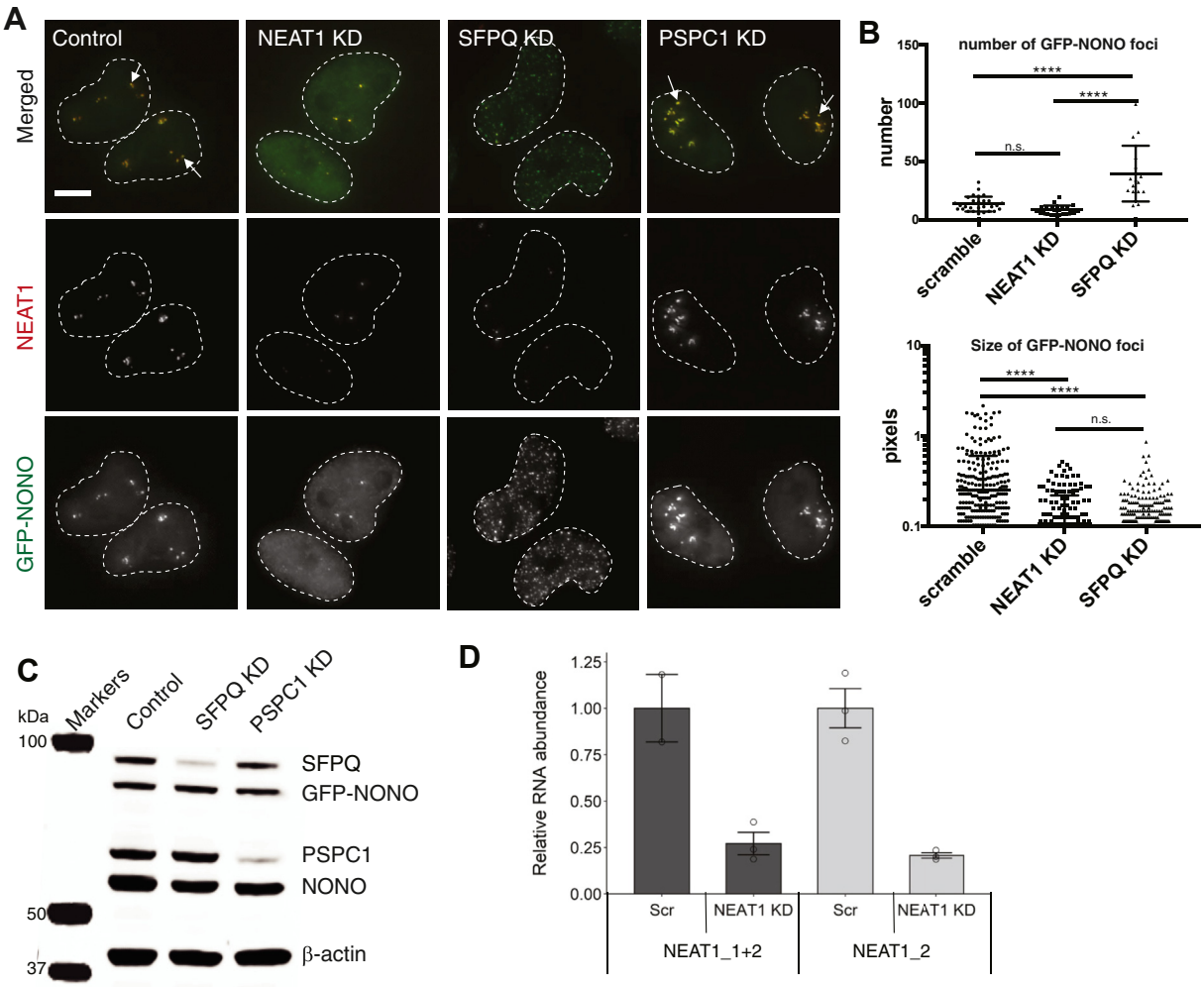

Figure 5. Differential relocalization patterns of GFP-NONO in the nuclei of HeLa$^{GFP\text{-}NONO}$ cells upon RNAi treatments that knockdown (KD) individual core components of paraspeckles. *A*, representative fluorescence micrographs of fixed HeLa$^{GFP\text{-}NONO}$ cells treated with (from *left* to *right*): control siRNA, showing distinct paraspeckles marked by GFP-NONO; NEAT1 siRNA showing predominant dispersion of GFP-NONO; SFPQ siRNA showing relocalization of GFP-NONO into random nuclear aggregates; and PSPC1 siRNA showing GFP-NONO persisting in paraspeckles. The *top panels* are fluorescent micrographs displaying both GFP-NONO (*green*) and NEAT1 (*red*), hence displaying *yellow* paraspeckles where GFP-NONO and NEAT1 are colocalized. The *bottom* two panels display NEAT1 signal only (*grayscale*, *middle*) and GFP-NONO (*grayscale*, *bottom*). Cell nuclei have been outlined with reference to DAPI nuclear signal. The scale bar represents 10 μm. *Arrows*, paraspeckles. *B*,quantitation of the number of GFP-NONO foci per nucleus (*top*) and individual size of each GFP-NONO foci (*bottom*) for each of the control/scramble, NEAT1 and SFPQ siRNA conditions as indicated. A minimum of 50 nuclei (technical replicates) were imaged and analyzed for each condition. **** $p < 0.00001$ by 1-way ANOVA. *C*, Western Blot showing protein abundance changes for siRNA reduction of paraspeckle proteins as indicated, using protein lysates samples harvested in parallel to the cells shown in (*A* and *B*). Molecular weight markers (kDa) are at left. Anti-NONO antibody was used to probe for GFP-NONO (82 kDa) and endogenous NONO (55 kDa). Anti-SFPQ (∼90 kDa) and Anti-PSPC1 (∼70 kDa) were used to show the abundance of these proteins. Beta actin (45 kDa) was used as the loading control. *D*, RT-qPCR of control/scramble and NEAT1 siRNA KD of RNA samples harvested in parallel wells to the cells/samples used in (*A–C*), using primers that overlap both NEAT1 isoforms 'NEAT1_1 + 2', or NEAT1_2 specific primers 'NEAT1_2' and normalizing to U6 housekeeping gene. Individual data points are technical replicates. Bars are SEM. Panels (*A–D*), one of three biological replicates. DAPI, 4′,6-diamidino-2-phenylindole; RT-qPCR, real-time quantitative PCR.

contains a single heterodimer with 2-fold noncrystallographic rotational symmetry, as described for the other two DBHS heterodimers (3, 7) (Fig. 6, *C–E*). The extensive dimerization interface is composed of interactions between the RRM2 domain of one partner and the NOPS domain of the other, which wraps around the outside of its respective partner RRM2, followed by an antiparallel right-handed coiled-coil formed by the α6 helices at the C terminus of each partner. In addition, the RRM1 domains pack against one another *via* their α2 helices—an interaction likely involved in determining their relative orientations.

We compared the NONO-SFPQ structure with the NONO homodimer (PDB 5ifm) and the NONO-PSPC1 heterodimer (PDB 3sde) and noted that although the overall domain architecture is the same, superposition highlights conformational differences in the coiled-coil, NOPS domain, and RRM1 domain, which may contribute to their partner preference, RNA specificity, and subnuclear localization.

Previous studies suggest structural plasticity in the NOPS domain and coiled-coil part of the dimerization domain is associated with conformational changes in specific residues at the dimer interface. This structural plasticity is readily apparent in the crystal of the NONO homodimer, where six independent NONO homodimers were observed (5), and is also indicated from structural comparisons between other DBHS protein crystal structures. Residues 245 to 250 of NONO NOPS form a

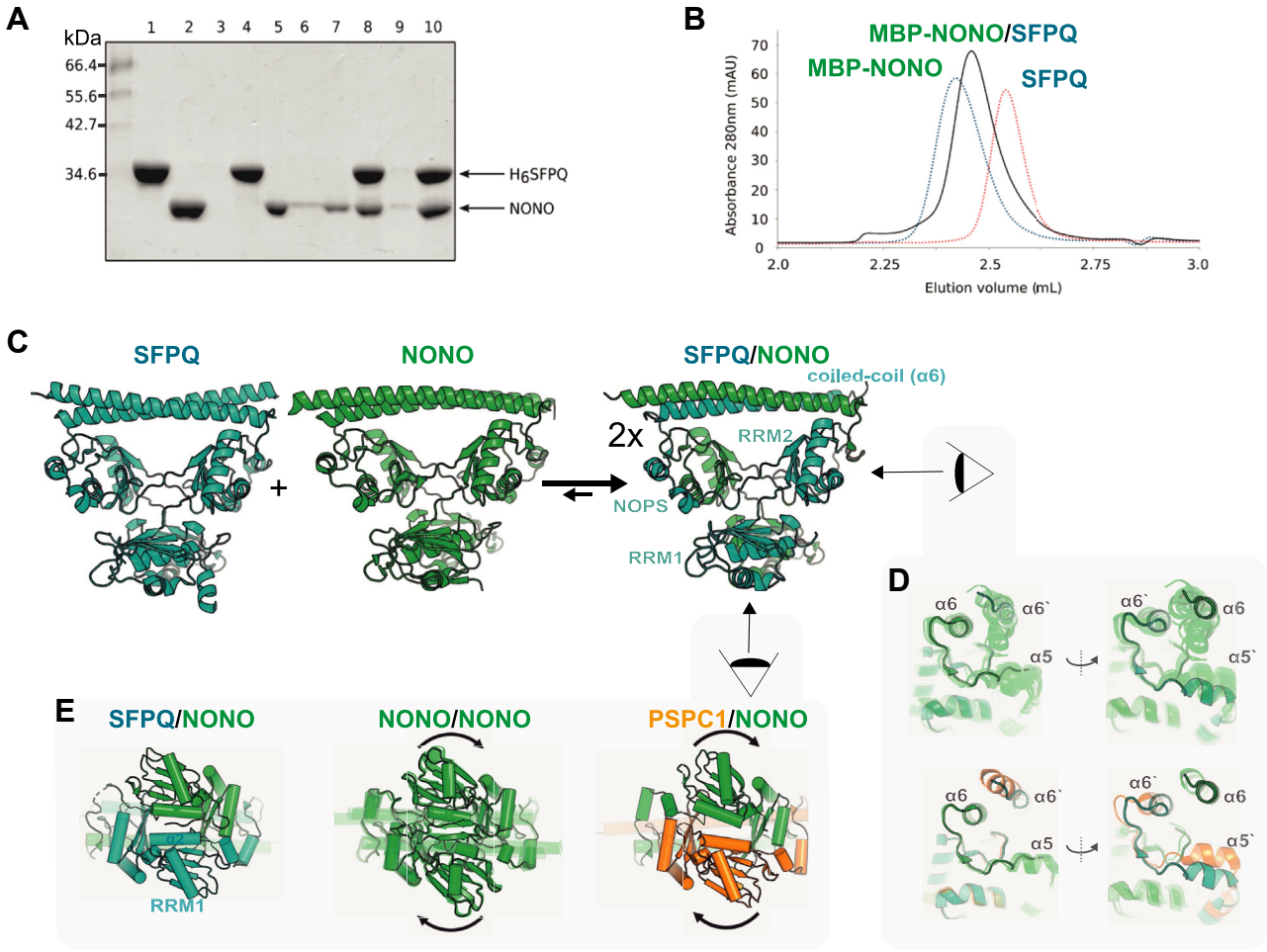

Figure 6. Assessing DBHS protein partner swapping by Ni-affinity pull downs, analytical size-exclusion chromatography, and structural comparisons. *A*, polyacrylamide gel of H_6SFPQ and NONO, showing pull down of NONO. 1: H_6SFPQ, 2: NONO, 3: H_6SFPQ Ni-affinity flow through, 4: H_6SFPQ Ni-affinity elution, 5: NONO Ni-affinity flow-through, 6: NONO Ni affinity elution, 7: H_6SFPQ and NONO incubated 1:1 at ambient temperature flow-through, 8: H_6SFPQ and NONO incubated 1:1 at ambient temperature elution, 9: H_6SFPQ and NONO incubated 1:1 at 37 °C flow through, 10: H_6SFPQ and NONO incubated 1:1 at 37 °C elution. *B*, analytical size-exclusion profile of MBP-NONO (*dashed blue*), SFPQ (*dashed red*), and MBP-NONO/SFPQ heterodimer (*solid black*). *C*, cartoon representation of SFPQ homodimer (4wii, *cyan*) mixed with structured NONO homodimer (5ifm, *green*) resulting in NONO-SFPQ heterodimer (7lrq). *D*, view down the longitudinal axis of the coiled-coil reveals structural differences in the NOPS domain (α5 helix) and distal coiled-coil (α6 helix) on both sides of the dimer. *Top*: NONO-SFPQ heterodimer superposed with NONO homodimer; bottom: NONO-SFPQ superposed with NONO-PSPC1 heterodimer. *E*, view from below (down the 2-fold axis of the dimer) shows that, relative to NONO-SFPQ, the RRM1 domains of both the other NONO-containing dimers are rotated ∼10° to 20° clockwise. Proteins are shown in cartoon representation, with NONO colored *green*, SFPQ *cyan*, and PSPC1 *orange*. All six dimers of the NONO homodimer are superposed in both orientations in (*D*) and (*E*). Helices are shown as cylinders in (*E*).

short α-helix (α5) in all 12 monomers in the NONO homodimer crystal (Fig. 6*D*, left, top) and in PSPC1-NONO (Fig. 6*D*, left, bottom) and are ∼15 Å from the distal coiled-coil of the partner subunit. In contrast, in NONO-SFPQ, residues 243 to 248 of NONO NOPS are highly disordered and do not form the α5 helix (Fig. 6*D*, left). This flexibility is reflected in the coiled-coil of SFPQ in the NONO-SFPQ heterodimer, with the seven C-terminal residues of SFPQ (529–535) also disordered, resulting in SFPQ helix α6 being two helical turns shorter than NONO, as it appears in the NONO homodimer and PSPC1 in NONO-PSPC1. In contrast, the NOPS domain of SFPQ is well ordered, with residues 469 to 474 forming the α5 helix (Fig. 6*D*, right). However, relative to NONO and PSPC1, this helix is positioned 3 to 6 Å further from the distal coiled-coil of its NONO partner. Together, these helices (NOPS α5 and the distal end of α6) form a major component of the dimerization interface. In addition, structural studies on SFPQ have shown that the α6 helix extends 60 residues beyond the coiled coil presented here and mediates the formation of DBHS polymers (6) (Fig. 1*B*). Control of this polymerization is critical to the gene regulatory functions and localization of SFPQ. Therefore, sequence-dependent conformational preferences in these regions could both determine dimer partner preference and stability and also have effects on the formation of polymeric protein–nucleic acid complexes.

The RRM1 domains of the DBHS dimer pack against one another *via* mutual interaction of their respective amphipathic α2 helices. Relative to NONO-SFPQ, the RRM1 domains of the NONO homodimer are rotated ∼15° such that the register of the α2 helices from each partner subunit is shifted by one helical turn with respect to the another (Fig. 6*E*). A similar shift in RRM1 orientation is observed for PSPC1-NONO. Differences in RRM1

orientation within, and between, different DBHS protein dimers have been noted previously (3, 7). Given the essential role that RRM1 plays in RNA binding (5) small changes in its orientation may influence RNA-binding affinity and/or specificity, potentially leading to differential localization within the cell nucleus. In the NONO homodimer, another structural feature observed at the N terminus of RRM1 is a short antiparallel β-sheet (Fig. 6*E*, centre) that is absent in SFPQ homodimer and PSPC1-NONO (Fig. 6*E*, right). This short NONO homodimer–specific 'β-clasp' contributes to high affinity interaction with particular nucleic acids *in vitro* (5). In contrast, for NONO-SFPQ, the N terminus of SFPQ is disordered (residues 276–289), and the corresponding N terminus of NONO in the heterodimer is poorly ordered and packs loosely against the α2 helices at the base of the RRM1 domains (Fig. 5*E*, left). Thus the 'β-clasp' is also missing in NONO-SFPQ, as in the other heterodimers. Overall, the NONO-SFPQ heterodimer has unique structural features at the N terminus of RRM1, the orientation of RRM1, and around the NOPS, each of which may contribute to nucleic acid binding and stability of this preferred DBHS heterodimer.

Discussion

Here, we have combined cellular and structural studies to characterize the DBHS protein NONO. We show cells with inducible GFP-NONO expression are an effective tool for paraspeckle dynamic assays, and observe with live-cell super-resolution imaging that linked chains of paraspeckle units can twist and flex over time, illustrating the constraints of the nuclear interchromosomal space. We also used these cells to reveal NONO dependence on SFPQ as a functional hetero-dimerization partner, with rapid dimer partner exchange. Despite an extensive DBHS dimerization interface, dynamic partner swapping *in vitro* and *in vivo* is nevertheless observed. The crystal structure of NONO-SPFQ heterodimer and structural comparison with other DBHS dimer combinations helps explain how NONO becomes relatively more disordered and flexible when in partnership with SFPQ. Thus, the increased flexibility of the NONO-SFPQ dimer may have been harnessed in evolution for specific gene regulatory roles, including paraspeckle formation.

3D-SIM is a super resolution microscopy technique that improves standard fluorescence microscopy resolution 2-fold to reveal 120 nm level detail. Whilst 3D-SIM has been used extensively for paraspeckles in fixed cells (14, 20) here, we used 3D-SIM longitudinal live-cell imaging experiments to reveal dynamic paraspeckles with torsional changes in orientation of the paraspeckle 'ends' with respect to each other. For one paraspeckle, the shape morphs from a 'C' to an 'S' shape. For another paraspeckle, over time, the ends move closer together to form a ring, composed of either three or four paraspeckle units. These 3D-SIM images are reminiscent of electron microscopy images of elongated paraspeckles (22). Thus 3D-SIM, even limited to 120 nm resolution can approximate electron microscopy observations with a resolution of 5 nm. In these experiments, it was a challenge to keep the cells alive, presumably due to severe phototoxicity resulting from the numerous images required for 3D-SIM for each z-section for each time point. Whilst several other studies have used 3D-SIM for live cell imaging (24, 25), very few have imaged cultured mammalian cells longitudinally for a significant amount of time. Future experiments with gentler lattice light sheet live cell experiments could extend these initial observations. As with 3D-SIM experiments on paraspeckles in fixed cells, we observe paraspeckles in different forms, including those that appear as 'singlet', 'doublet', and 'multiplet' GFP-NONO units (*e.g.*, Fig. S3). The molecular stoichiometry of paraspeckles is yet to be fully determined. Although an individual paraspeckle unit contains approximately 50 NEAT1_2 molecules (26), the number of protein molecules in each unit or the relative protein amounts in the core *versus* the shell of the paraspeckle is not known. It should be noted that as NONO is found at the core of the paraspeckle, our imaging is only able to reveal the dynamics of the paraspeckle core and not the shell.

The significance of these flexions and torsions in paraspeckle morphology is unknown. Nor is it known what factors limit the overall length that a paraspeckle can obtain. The nucleus is a dynamic environment for molecular diffusion, with high rates of exchange for molecules between compartments (27). However, the nucleus is also extremely crowded, and few studies have investigated how this crowding might impact the flexibility of nuclear bodies. Some nuclear bodies (*e.g.*, Cajal bodies, PML bodies) move throughout the interchromatin space (28), however, these are generally smaller than paraspeckles and overall spherical. Nuclear speckles are more amorphous in size but do not have mobility. It would be interesting in future experiments to deplete ATP levels to determine if the flexibility we observe requires energy or is a more passive process responding to nuclear distortions.

The subnuclear localization of nuclear proteins is increasingly being recognized as important in determining specificity of function for gene regulatory proteins. For example, nuclear stress bodies sequester and alter the function of splicing factors (29) and other lncRNA-seeded structures trap RNA-binding proteins influencing their target gene levels (30). For nuclear proteins, there is thus a dynamic interchange between different nuclear structures, likely dictated by molecular affinity for substrate molecules that form the backbone of the nuclear structure. For DBHS proteins, it appears NEAT1 RNA is the highest affinity nuclear substrate under steady state conditions, as GFP-NONO is targeted to paraspeckles soon after being imported into the nucleus. The nucleoplasmic 'pool' appears to be the other major site of GFP-NONO and DBHS localization. Although DBHS proteins have an important structural role in paraspeckle formation (13), there is only one reported functional activity for DBHS proteins in paraspeckles, related to enhanced processing of pri-miRNA (17). Outside the paraspeckle, the nucleoplasmic pool of DBHS proteins likely enacts a multitude of functions, from transcriptional control to splicing and DNA repair (4). In addition, DBHS proteins have a small steady-state cytoplasmic pool that plays significant roles in the neuronal context (31). Finally, when RNA Polymerase II transcription is not active (for

example, during telophase) or is artificially inhibited with drug treatment, the site for DBHS protein accumulation is the nucleolus, specifically nucleolar cap structures (2, 8).

Others have previously shown that SFPQ is the key protein to direct localization of the NONO-SFPQ dimer to sites of DNA damage (32) and SFPQ is responsible for the recruitment of NONO-SFPQ to mRNAs in complex with Agos2 and miRNAs in the RISC complex (33). Here, we also show the subnuclear localization of NONO is directed by its dimerization partner. In the absence of paraspeckles, NONO-SFPQ (diffuse nuclear) has a very different localization to NONO homodimer or NONO-PSPC1 (numerous small aggregates). Features of SFPQ, but not NONO, are likely required for the recruitment of NONO-SFPQ to DNA damage sites, RISC-loaded mRNAs and paraspeckles. Reflecting potential diverse function for each possible dimer combination, all three DBHS proteins are classified as having very low tolerance of loss of function in the human genome (34). Thus, all three DBHS proteins likely play unique roles in human physiology.

DBHS proteins are obligate dimers, with dimerization driven by reciprocal interactions between the RRM2, NOPS, and coiled-coil domains. Despite high similarity in these domains between NONO, SFPQ, and PSPC1, there is nevertheless a preference for existing as heterodimers, rather than homodimers. Our partner swapping experiments show that NONO and SFPQ homodimers, when mixed, readily form NONO-SFPQ heterodimers. The X-ray crystal structure of NONO-SFPQ, presented herein, has allowed us to compare all three NONO-containing DBHS dimers and again highlights the intimate association of DBHS partners at their dimerization interface. Of note, the complete unwrapping of the NOPS domain from the RRM2 domain of its dimeric partner would be required for partner exchange. The structural variation that we observe in the NOPS domain of the three NONO-containing dimers hints at an inherent structural plasticity in this region that may be necessary to allow for dynamic exchange of DBHS partners. By our structural comparison, we have also identified conformational variability in the RRM1 domain and distal coiled coil—regions that are essential for RNA binding and oligomerization of DBHS dimers, respectively (5, 6). Given the close spatial arrangement of the NOPS domain and distal coiled coil of dimeric partners, it is possible that partner identity, frequency of dimer partner exchange, and oligomeric state are all coupled. Small sequence variations that are present in these regions may cause subtle shifts in conformational preference, influencing both nucleic acid interactions and protein oligomerization, providing a molecular mechanism for dimer-specific localization and function(s) within the cell.

We have been cautious about overinterpreting our structural data, as the structural features of interest are all at the periphery of the protein dimer and therefore possibly liable to be influenced by contact with neighboring molecules in the crystal lattice. However, while this article was in preparation, Schell *et al.* independently reported a crystal structure of the NONO-SFPQ heterodimer (PDB ID 7pu5), which increases our confidence in our conclusions (35). Despite having different crystal packing (space group *C*121), a lower resolution (3.00 Å), and more molecules in the asymmetric unit (six NONO-SFPQ dimers), this alternate structure is nearly identical to ours (Fig. S4), suggesting that the structural variation we observe is indeed DBHS partner specific. The only notable difference between 7pu5 and our structure (7lrq) concerns the α5 helix of NONO (residues 245–250), which is relatively well ordered in 7pu5, in contrast to 7lrq, where it is disordered. These residues are at a 2-fold rotation axis in both crystals, such that they interact their counterpart residues in the neighboring molecule. In 7pu5, the NONO α5 helix counterparts pack loosely against one another, whereas in our crystal, the molecules are more tightly packed, forcing the residues of this region (∼240–250) to occupy the same space, disrupting the helix. We suggest that this further highlights the apparent structural plasticity of the NOPS domain, which would be important for allowing the dynamic partner exchange we observe for DBHS dimers.

It is interesting to speculate about the roles of the low complexity sequences at the N and C termini of DBHS proteins in directing localization and function of dimer pairs. SFPQ has an extended low sequence complexity domain at the N terminus, enriched in proline and glutamine residues, whereas all three DBHS proteins have C-terminal low complexity regions, of various compositions and lengths (Fig. 1*A*). These low complexity domains are likely driving LLPS as has been demonstrated for numerous other low complexity domains in gene regulatory proteins. LLPS is speculated to be important, not just in forming large microscopically visible bodies, such as paraspeckles, nucleoli, and DNA damage foci (36), but also potentially important for recruiting RNA polymerase II to transcription sites (37). Future experiments addressing the roles of these low complexity regions in DBHS and paraspeckle biology will be important.

Overall, this study describes a new tool for imaging paraspeckles in living cells. Given the emerging roles of paraspeckles in a variety of stress-related and disease contexts, this ability to study and potentially modulate paraspeckle dynamics will be increasingly important. Further, this study reveals the importance of SFPQ for targeting DBHS dimers to different nuclear locations. Given the multifunctional nature of the DBHS protein family, it is critical to tease apart distinct roles for different members of the family.

Experimental procedures

HeLa$^{GFP\text{-}NONO}$ cells and cell culture

To generate the HeLa$^{GFP\text{-}NONO}$ cell line, HeLa cells were first transfected with pCMV–Tet3G transactivator vector (Clontech Laboratories) and a stable cell line expressing the transactivator, named Tet-ON 3G HeLa, was selected with G418 (MP Biomedicals). GFP-NONO (a fusion of *Homo sapiens* NONO complementary DNA [cDNA] and the tagGFP cDNA at the N terminus, hereafter called GFP-NONO) was then cloned into the pTRE3G response vector (Clontech) to form the P_{TRE3G}–GFP–NONO plasmid. Tet-ON 3G HeLa

were then cotransfected with the P_{TRE3G}–GFP–NONO plasmid and a linear puromycin marker (Clontech). Colonies of the successfully transfected cells were then selected for with 200 μg/ml G418 (MP Biomedicals), 0.5 μg/ml puromycin (Sigma), and 50 ng/ml Dox (Sigma). Single colonies were then tested for optimal expression and one was named $HeLa^{GFP\text{-}NONO}$ cells and used in the experiments described in this study.

$HeLa^{GFP\text{-}NONO}$ cells were routinely cultured in Dulbecco's modified Eagle's medium (DMEM) (Gibco) supplemented with 10% fetal calf serum (FCS) (Gibco), 1% penicillin streptomycin (Invitrogen), 200 μg/ml of G418, and 0.5 μg/ml of puromycin. For indirect immunofluorescence, cells were grown on glass coverslips (VWR International) in DMEM/10% FCS and no antibiotics. For live-cell imaging experiments, cells were grown in wells of the 8-well μ-Slide (ibidi) in DMEM/10% FCS and no antibiotics. Expression of GFP-NONO was induced with the addition of Dox (Sigma) at the concentrations and durations indicated in each experiment.

Protein extraction and Western blotting

$HeLa^{GFP\text{-}NONO}$ cells were rinsed with PBS (Invitrogen) and lysed using 1× Passive Lysis Buffer (Promega). Samples were then spun at 6000 rpm for 1 min at room temperature (RT). The concentration of protein in supernatant was quantified using the Bio-rad Bradford protein assay (Bio-Rad) and 50 mg of protein in each sample was precipitated with 5× volume of acetone at −80 °C overnight, thawed on ice, and centrifuged at 1300*g* for 1 h at −4 °C. After removal of acetone supernatant, the precipitated protein extract in the pellet was dissolved in SDS sample buffer (5% glycerol, 2% SDS, 62.5 mM Tris–HCl, pH 6.8, 2% 2-mercaptoethanol, 0.01% bromophenol blue) at 70 °C for 10 min. Protein extracts (50 μg/lane) and protein standards (Bio-Rad) were then separated on 4% to 12% Bis–Tris gels (Invitrogen). Separated proteins were transferred onto nitrocellulose membrane (Millipore) using a XCell II Blot Module (Invitrogen) and transfer buffer containing 12 mM Tris, 100 mM glycine, and 20% methanol, followed by blocking with 5% skim milk powder in PBS + 0.05% Tween 20 (PBS-T). Immunoblotting was performed by incubating membrane with various combinations of primary antibodies: mouse anti-NONO (1:10,000 (19)), rabbit antiactin (1:10,000; Sigma, A2066), mouse antiactin (1:10,000; [AC-15] Abcam), mouse anti-SFPQ (1:1000; Sigma, B92, P2860), and rabbit anti-PSPC1 (1:10,000; Sigma, SAB4200068) for 1 h, followed by probing with IRDYE 680RB donkey antimouse IgG (1:5000; LI-COR, P926-68072) and/or IRDYE 800CW donkey anti-rabbit IgG (1:5000; LI-COR, P926-32213) in PBS containing 5% milk powder and 0.05% Tween 20 and detected *via* the Odyssey Infrared Imaging System (LI-COR) at 680 nm and/or 800 nm.

Analysis of NEAT1 levels by quantitative real-time PCR

Total RNA were isolated at 24 h post-transfection using the TRIsure reagent (Bioline) from NEAT1 siRNA-transfected cells, according to manufacturer's instructions. The concentration and purity of total RNA was determined by NanoDrop ND-1000 Spectrophotometer (NanoDrop Technologies, Inc). Hundred nanograms of total RNA was reverse transcribed using the QuantiTect Reverse Transcription Kit (QIAGEN Inc). Real-time PCR was performed on cDNA samples using the SensiFAST SYBR Hi-ROX Kit (Bioline) on a Rotor Gene real-time PCR machine (Corbett Research) to quantify the levels of a mixture of both long and short isoforms of NEAT1 (NEAT1_v1v2) and the long isoform of NEAT1 only (NEAT1_v2). U6 was used as the housekeeping gene. Sequences of primers (forward, reverse) used are as follows: NEAT1_1 + 2 (GTGGCTGTTGGAGTCGGTAT, TAACA AACCACGGTCCATGA), NEAT1_2 (GTCTTTCCATCCAC TCACGTCTATTT, GTACTCTGTGATGGGGTAGTCAGT CAG), and U6 (CTCGCTTCGGCAGCACA, AACGCTTCAC GAATTTGCGT). Results of quantitative PCR assays were analyzed using software supplied with the Rotor Gene machine.

Indirect immunofluorescence for endogenous NONO

$HeLa^{GFP\text{-}NONO}$ cells that were either expressing GFP-NONO or uninduced by Dox were seeded at approximately 70% confluency and fixed for 5 min in 4% paraformaldehyde (in PBS) and washed thrice with PBS. Cells were permeabilized in 1% Trition X-100 for 15 min, washed thrice with PBS, and once with PBS-T (as aforementioned). Cells were stained with mouse anti-NONO (1:500 (19)) in PBS-T for 1 h, washed thrice in PBS-T, and then incubated with secondary antibody Alexafluor 648 (AF648)-conjugated Donkey antimouse IgG (Jackson ImmunoResearch, 711-025-152) for a further 1 h, washed thrice, and counterstained with 4′,6-diamidino-2-phenylindole (DAPI) (0.3 mg/ml, Sigma) for DNA labeling for 1 min, washed once with PBS, and finally mounted using Vectashield (Vector Laboratories).

NEAT1-RNA FISH

$HeLa^{GFP\text{-}NONO}$ cells, uninduced or expressing GFP-NONO, were seeded at approximately 70% confluency on the day prior to fixation, then fixed for 10 min in 4% paraformaldehyde (in PBS), and washed once with PBS. Cells were permeabilized in 70% ethanol for at least 1 h at 4 °C and washed once with wash buffer for 5 min. Wash buffer was prepared with 10% formamide (Ambion) in 2× SSC (contains 0.3 M of NaCl and 30 mM of sodium citrate). Hybridization buffer was prepared with 100 mg/ml dextran sulfate (Sigma) and 10% formamide in 2× SSC. A hybridization mixture was prepared using 125 nM of Stellaris FISH Probes (Biosearch Technologies, Inc) targeted to the long isoform of human NEAT1 labeled with Quasar 570 Dye (SMF-2037-1, Biosearch), made to a final concentration of 100 mg/ml dextran sulfate, 10% formamide, and 2× SSC. Each coverslip was transferred onto a 50 μl drop of hybridization mixture, cells side down, incubated in a sealed, dark humidified chamber overnight at 37 °C. Coverslips were then rinsed with wash buffer for 30 min at 37 °C in the dark, counterstained with DAPI (5 ng/ml in wash buffer) for 30 min at 37 °C in the dark, and finally rinsed in 2× SSC. Coverslips were mounted onto microscopic slides using Vectashield mounting medium.

siRNA transfection for RNAi

siRNAs targeting SFPQ (siGENOME SMARTpool, [M-006455-02]) and PSPC1 (siGENOME SMARTpool, [M-020596-01]) were purchased from GE Healthcare Dharmacon Inc. siRNAs targeting NEAT1 (*Silencer* Select Human NEAT1 siRNA, [4390771]; Ambion) and negative control (*Silencer* Select Negative Control No. 1 siRNA, [4390844]; Ambion) were also used. siRNA transfections of HeLa$^{GFP\text{-}NONO}$ in the RNAi treatments were performed with Lipofectamine 2000 (Invitrogen), according to the manufacturer's protocol. Briefly, for a 12-well format (100,000 cells were seeded per well), 2 μl of Lipofectamine 2000 was diluted in 100 μl of optiMEM medium (Gibco). About 40 pmol of each siRNA was then diluted in 100 μl of optiMEM medium and incubated at RT for 5 min. The diluted Lipofectamine 2000 and diluted siRNA were then mixed and incubated at RT for 30 min. siRNA-Lipofectamine complexes were then directly added to seeded cells, mixed gently, and incubated at 37 °C for approximately 4 h; siRNA-Lipofectamine complexes were then removed and replaced with fresh HeLa media.

Fluorescence microscopy

Fixed cells, treated as aforementioned, were imaged using a fluorescent microscope (Nikon TiE) with the FITC, TRITC, and DAPI filters and with a 60× objective lens. Z-stack projection (NIS-Element software) was used for all instances and sections at 0.3 μm intervals were obtained throughout each cell nucleus, each with approximately 500 ms exposure time.

For live-cell microscopy, HeLa$^{GFP\text{-}NONO}$ cells were seeded at approximately 50% confluency the day prior to imaging in wells of a μ-Slide, then were fitted into the prewarmed environmental chamber (Tokai-Hit) fixed to the microscope and allowed to equilibrate at 37 °C on the day of imaging. The environmental chamber was connected to a Tokai-Hit control unit providing constant 37 °C and 5% CO_2 for the living cells. Multiple x, y stage points were selected and focused using the Nikon Perfect Focus System to prevent any inherent focus drift. At each time point, 11 Z-sections at 1.0 μm intervals were obtained through each cell, each with 50 ms and 10 ms exposure times using the FITC and brightfield filters, respectively. When needed, DNA in live cells was labeled by preincubation with HeLa media containing 0.15 μg/ml Hoechst 33342 (Invitrogen) for 30 min, followed by replacement with fresh HeLa media. Cells were allowed to recover for 30 min before imaging as described previously. Fluorescence signal from Hoechst was captured using the DAPI filter at 50 ms exposure.

Super-resolution microscopy

Both fixed and live cells were imaged using the DeltaVision OMX V4 Blaze-SIM system (Applied Precision). Images were acquired using the 60X 1.42 NA objective lens. Before every experiment, a reference image using TetraSpeck fluorescent beads (Life Technologies) was taken and used to correct for chromatic aberrations. Immersion oil with a refractive index between 1.512 and 1.516 was used to match refractive indexes with the mounting media to minimize the effect of spherical aberrations. For microscopy on fixed cells, Z series images were taken at 4.5 μm optical thickness with a 0.125 μm interval. Images were taken with varying exposure times using the DAPI (BP436/31), 488 (BP478/35) and A568 (BP609/37) filters. Raw data were reconstructed, aligned, and a maximum intensity projection was applied on all images using the Softworx software (Applied Precision).

For live-cell experiments, μ-slides were fitted on the stage at a constant environment of 37 °C and 5% CO_2. Multiple x, y stage points were selected at the start of each experiment. At each time point, cells at every stage point were focused manually to minimize inherent focus drift, followed by taking Z series images of a total optical thickness of 3 μm with 0.125 μm intervals. Images were taken at 5 ms exposure, using the 488 filter (BP478/35). Raw data were processed as aforementioned.

Image analysis

Quantification of GFP-NONO foci in fixed cell imaging was carried out using FIJI software (38). Briefly, maximum intensity projections were generated and the nuclear boundary determined with DAPI thresholding. The number of GFP-NONO foci within each nucleus was then determined by thresholding the green fluorescence intensity, and the size of each thresholded foci was measured in pixels. The same threshold values were used across all images. A minimum of 50 nuclei were measured for each condition.

3D image analysis was first conducted on raw images taken from live-cell experiments, using the Imaris (Bitplane) software. The surface detection method was used to create 3D structures GFP-NONO–labeled paraspeckles based on FITC fluorescence. The threshold was manually determined as the brightest background and applied to all images identically. Values of the volume and surface area of resultant 3D structures were obtained from Imaris-generated statistics. To correct movements of imaged cells in between time points, Imaris-generated 3D structures of GFP-NONO–labeled paraspeckles obtained from every time point were aligned with the help of the 'translate' function of Blender (blender.org), an open source software. Blender was also used to render 3D visualizations of individual paraspeckles of interest.

MG132 treatment

To encourage growth of paraspeckles over time, MG132-induced stress, which increases transcription of NEAT1 (22), was applied by adding MG132 (Sigma) to a final concentration of 1 μM to cells 30 min prior to the start of live-cell imaging.

X-ray crystallography

Recombinant heterodimer containing only the core DBHS regions of SFPQ (aa 276–535) and NONO (aa 53–312) was purified as in (6). Briefly, *E. coli* Rosetta 2 (DE3) (Merck Millipore) cells harboring pETDuet-1-NONO(53–312) (coding sequence for NONO inserted at second multiple cloning site, resulting in expression of untagged NONO) and pCDF-11-SFPQ(276–535) were grown in 0.5 l LB broth at 37 °C in shake flasks. At an A_{600} of ∼0.5, 0.5 mM IPTG was added to

induce coexpression of untagged NONO(53–312) with hexahistidine-tagged (H_6) SFPQ(276–535) for 16 h at 25 °C. Harvested cells were resuspended in 50 ml Ni-binding buffer (1 M NaCl, 25 mM imidazole, 10% *v/v* glycerol, 50 mM Tris–HCl pH 7.5) supplemented with 5 μl DNase I (10 units, New England Biolabs) and lysed using an Avestin C5 homogenizer. H_6-tagged protein was isolated from clarified bacterial lysate by Ni^{2+}-affinity chromatography using a 5 ml HisTrap HP column (Cytiva) and eluted using a 25 to 500 mM imidazole gradient. H_6-tagged protein eluted from the column in two distinct peaks. SDS-PAGE analysis showed that the first peak (at lower [imidazole]) contained SFPQ-NONO heterodimer and the second peak SFPQ homodimer, as described previously (6). SFPQ-NONO peak fractions were pooled, diluted 1/3 with gel filtration buffer (250 mM NaCl, 50 mM L-Proline, 0.5 mM EDTA, 20 mM Tris–HCl pH 7.5), subjected to TEV protease digestion overnight at RT (1:50 *w/w* TEV:SFPQ-NONO), and passed back through the Ni^{2+}-affinity column to remove the cleaved H_6-tag. The sample volume was then reduced to ∼5 ml using a 10,000 MWCO centrifugal filter device (Amicon) and passed through a HiLoad 16/60 Superdex 200 column (GE Healthcare) equilibrated in gel filtration buffer. Peak fractions were concentrated to 10 mg/ml, flash frozen in liquid nitrogen, and stored at −80 °C.

Screening for crystallization by vapor diffusion was performed in 96-well sitting drop format at 20 °C using a range of commercially available sparse-matrix screens. Small rhombohedral crystals were observed in conditions G11, G12, and H1 of Index HT (Hampton Research), all of which contain 0.2 M $MgCl_2$, 25% *w/v* PEG 3350 with 0.1 M Bis–Tris pH 6.5, 0.1 M Hepes pH 7.5, or 0.1 M Tris pH 8.5, respectively. Subsequent optimization of these conditions in hanging drop format yielded larger, reproducible crystals. Rhombohedral crystals grew to a maximum size of ∼200 μm in less than 3 days in 2 μl drops containing equal volumes of reservoir and protein sample, over a 0.5 ml reservoir composed of 22.5% PEG 3350, 0.4 M $MgCl_2$, 0.1 M Hepes pH 7.5. Single crystals from this condition were flash frozen in liquid nitrogen using Paratone-N (Hampton Research) as cryoprotectant. X-ray diffraction data were collected at the Australian Synchrotron MX1 beamline (39) at 100 K, 13,000 eV. Three separate datasets were collected at different detector distances from a single crystal, each consisting of 360 frames, with each frame capturing a 1 s exposure through a phi angle of 1°. Datasets were indexed using XDS (40), combined using *BLEND* (41) and scaled and merged using *AIMLESS* (42) in space group $P3_121$. The structure was solved by molecular replacement with 4wii as the search model using phaserMR (43). Refinement of atomic coordinates was performed in phenix.refine (44) using data to 2.3 Å, with iterative rounds of manual rebuilding using Coot (45). Anisotropic refinement was restricted to automatically defined translation-libration-screw (TLS) groups. Data collection and refinement statistics are listed in Table S1.

Ni-affinity pull down and analytical size exclusion

Hexahistidine-tagged (H_6) SFPQ (aa 276–535) and NONO (aa 53–312) were expressed and purified as in (6, 23), respectively. The protein purification protocol was essentially identical to the method described previously for crystallization of the heterodimer, with the exception that the plasmids were not cotransformed into the same *E. coli* but were grown as separate cultures. Also, the pETDuet-1 plasmid used for NONO (53–312) expression contained the NONO coding sequence at the first multiple cloning site, resulting in expression of H_6-tagged NONO. The H_6-tag was removed from NONO during purification, as described previously. Purified SFPQ and NONO homodimers were then incubated together at a 1:1 M ratio to allow for partner swapping at ambient temperature or at 37 °C for 1 h before application to a His SpinTrap (GE Healthcare). After washing with four column volumes of binding buffer (20 mM Tris-Cl pH 7.5, 250 mM NaCl, 25 mM imidazole, 10% v/v glycerol), bound protein was eluted in elution buffer (20 mM Tris-Cl pH 7.5, 250 mM NaCl, 500 mM imidazole, 10% v/v glycerol) and examined on a 12% (v/v) polyacrylamide gel stained with Coomassie Brilliant Blue R-250 (Amresco). Analytical gel filtration experiments were carried out by incubating purified SFPQ and MBP-NONO homodimers together at a 1:1 M ratio to allow for partner swapping at 310 K for 1 h. The incubated sample and SFPQ or MBP-NONO only controls were applied to a S200 5/150 gel filtration column (GE Healthcare) developed at 0.3 ml/min in gel filtration buffer (20 mM Tris-Cl pH 7.5, 250 mM NaCl, 10% v/v glycerol).

Data availability

Atomic coordinates and structure factors are deposited online at the RCSB Protein Data Bank under accession number 7LRQ.

Supporting information—This article contains supporting information (35).

Acknowledgments—This research was undertaken on the MX1 beamline at the Australian Synchrotron, part of ANSTO. We thank members of the Fox and Bond labs for useful discussions about this study.

Author contributions—L. M., M. L., C. S. B., and A. H. F. conceptualization; P. W. L., L. M., S. K., P. J. M., and M. L. methodology; E. C. formal analysis; P. W. L., A. C. M., G. J. K., L. M., and P. J. M. investigation; P. W. L., A. C. M., G. J. K., and A. H. F. writing–original draft; C. S. B. and A. H. F. writing–review & editing; P. W. L., A. C. M., G. J. K., S. K., C. S. B., and A. H. F. visualization; C. S. B. and A. H. F. supervision; A. H. F. project administration; A. H. F. funding acquisition.

Funding and additional information—This work was funded by the Australian Research Council (FT180100204 to A. H. F. and DP160102435 to C. S. B. and A H. F.) and the National Health and Medical Research Council of Australia (APP1147496 to C. S. B. and A. H. F.). This research was made possible by the Clifford Bradley Robertson and Gwendoline Florence Anne Robertson Research Endowment Fund, established through Dr Glen Robertson's bequest to The University of Western Australia (to A. M.).

Conflict of interest—The authors declare that they have no conflict of interest with the contents of this article.

Abbreviations—The abbreviations used are: cDNA, complementary DNA; DAPI, 4′,6-diamidino-2-phenylindole; DOX, Doxycycline; FCS, fetal calf serum; KD, Knock down; LLPS, Liquid Liquid Phase Separation; PDB, Protein Data Bank; RRM, RNA recognition motif; SIM, structured illumination microscopy.

References

1. Myojin, R., Kuwahara, S., Yasaki, T., Matsunaga, T., Sakurai, T., Kimura, M., *et al.* (2004) Expression and functional significance of mouse paraspeckle protein 1 on Spermatogenesis1. *Biol. Reprod.* **71**, 926–932
2. Fox, A. H., Bond, C. S., and Lamond, A. I. (2005) P54nrb forms a heterodimer with PSP1 that localizes to paraspeckles in an. *Mol. Biol. Cell* **16**, 5304–5315
3. Passon, D. M., Lee, M., Fox, A. H., and Bond, C. S. (2011) Crystallization of a paraspeckle protein PSPC1-NONO heterodimer. *Acta Crystallogr. Sect. F Struct. Biol. Cryst. Commun.* **67**, 1231–1234
4. Knott, G. J., Bond, C. S., and Fox, A. H. (2016) The DBHS proteins SFPQ, NONO and PSPC1: a multipurpose molecular scaffold. *Nucl. Acids Res.* **44**, 3989–4004
5. Knott, G. J., Chong, Y. S., Passon, D. M., Liang, X., Deplazes, E., Conte, M. R., *et al.* (2022) Structural basis of dimerization and nucleic acid binding of human DBHS proteins NONO and PSPC1. *Nucl. Acids Res.* **50**, 522–535
6. Lee, M., Sadowska, A., Bekere, I., Ho, D., Gully, B. S., Lu, Y., *et al.* (2015) The structure of human SFPQ reveals a coiled-coil mediated polymer essential for functional aggregation in gene regulation. *Nucl. Acids Res.* **43**, 3826–3840
7. Huang, J., Casas Garcia, G. P., Perugini, M. A., Fox, A. H., Bond, C. S., and Lee, M. (2018) Crystal structure of a SFPQ/PSPC1 heterodimer provides insights into preferential heterodimerization of human DBHS family proteins. *J. Biol. Chem.* **293**, 6593–6602
8. Fox, A. H., Lam, Y. W., Leung, A. K. L., Lyon, C. E., Andersen, J., Mann, M., *et al.* (2002) Paraspeckles: a novel nuclear domain. *Curr. Biol.* **12**, 13–25
9. Clemson, C. M., Hutchinson, J. N., Sara, S. A., Ensminger, A. W., Fox, A. H., Chess, A., *et al.* (2009) An architectural role for a nuclear noncoding RNA: NEAT1 RNA is essential for the structure of paraspeckles. *Mol. Cell* **33**, 717–726
10. Sasaki, Y. T. F., Ideue, T., Sano, M., Mituyama, T., and Hirose, T. (2009) MENε/β noncoding RNAs are essential for structural integrity of nuclear paraspeckles. *Proc. Natl. Acad. Sci. U. S. A.* **106**, 2525–2530
11. Chen, L.-L., and Carmichael, G. G. (2009) Altered nuclear retention of mRNAs containing inverted repeats in human embryonic stem cells: functional role of a nuclear noncoding RNA. *Mol. Cell* **35**, 467–478
12. Yamazaki, T., and Hirose, T. (2015) The building process of the functional paraspeckle with long non-coding RNAs. *Front. Biosci. Elite* **7**, 1–47
13. Naganuma, T., Nakagawa, S., Tanigawa, A., Sasaki, Y. F., Goshima, N., and Hirose, T. (2012) Alternative 3′-end processing of long noncoding RNA initiates construction of nuclear paraspeckles. *EMBO J.* **31**, 4020–4034
14. West, J. A., Mito, M., Kurosaka, S., Takumi, T., Tanegashima, C., Chujo, T., *et al.* (2016) Structural, super-resolution microscopy analysis of paraspeckle nuclear body organization. *J. Cell Biol.* **214**, 817–830
15. Sunwoo, H., Dinger, M. E., Wilusz, J. E., Amaral, P. P., Mattick, J. S., and Spector, D. L. (2009) MEN ε/β nuclear-retained non-coding RNAs are up-regulated upon muscle differentiation and are essential components of paraspeckles. *Genome Res.* **19**, 347–359
16. Prasanth, K. V., Prasanth, S. G., Xuan, Z., Hearn, S., Freier, S. M., Bennett, C. F., *et al.* (2005) Regulating gene expression through RNA nuclear retention. *Cell* **123**, 249–263
17. Jiang, L., Shao, C., Wu, Q.-J., Chen, G., Zhou, J., Yang, B., *et al.* (2017) NEAT1 scaffolds RNA-binding proteins and the microprocessor to globally enhance pri-miRNA processing. *Nat. Struct. Mol. Biol.* **24**, 816–824
18. McCluggage, F., and Fox, A. H. (2021) Paraspeckle nuclear condensates: global sensors of cell stress? *Bioessays* **43**, 2000245
19. Souquere, S., Beauclair, G., Harper, F., Fox, A., and Pierron, G. (2010) Highly ordered spatial organization of the structural long noncoding NEAT1 RNAs within paraspeckle nuclear bodies. *Mol. Biol. Cell* **21**, 4020–4027
20. Wang, Y., Hu, S.-B., Wang, M.-R., Yao, R.-W., Wu, D., Yang, L., *et al.* (2018) Genome-wide screening of NEAT1 regulators reveals cross-regulation between paraspeckles and mitochondria. *Nat. Cell Biol.* **20**, 1145–1158
21. Mao, Y. S., Sunwoo, H., Zhang, B., and Spector, D. L. (2011) Direct visualization of the Co-transcriptional assembly of a nuclear body by noncoding RNAs. *Nat. Cell Biol.* **13**, 95–101
22. Hirose, T., Virnicchi, G., Tanigawa, A., Naganuma, T., Li, R., Kimura, H., *et al.* (2014) NEAT1 long noncoding RNA regulates transcription *via* protein sequestration within subnuclear bodies. *Mol. Biol. Cell* **25**, 169–183
23. Knott, G. J., Lee, M., Passon, D. M., Fox, A. H., and Bond, C. S. (2015) Caenorhabditis elegans NONO-1: insights into DBHS protein structure, architecture, and function. *Protein Sci.* **24**, 2033–2043
24. Shao, L., Kner, P., Rego, E. H., and Gustafsson, M. G. L. (2011) Super-resolution 3D microscopy of live whole cells using structured illumination. *Nat. Met.* **8**, 1044–1046
25. Fiolka, R., Shao, L., Rego, E. H., Davidson, M. W., and Gustafsson, M. G. L. (2012) Time-lapse two-color 3D imaging of live cells with doubled resolution using structured illumination. *Proc. Natl. Acad. Sci. U. S. A.* **109**, 5311–5315
26. Chujo, T., Yamazaki, T., Kawaguchi, T., Kurosaka, S., Takumi, T., Nakagawa, S., *et al.* (2017) Unusual semi-extractability as a hallmark of nuclear body-associated architectural noncoding RNAs. *EMBO J.* **36**, 1447–1462
27. Phair, R. D., and Misteli, T. (2000) High mobility of proteins in the mammalian cell nucleus. *Nature* **404**, 604–609
28. Platani, M., Goldberg, I., Swedlow, J. R., and Lamond, A. I. (2000) *In vivo* analysis of Cajal body movement, separation, and joining in live human cells. *J. Cell Biol.* **151**, 1561–1574
29. Biamonti, G., and Vourc'h, C. (2010) Nuclear stress bodies. *Cold Spring Harb. Perspect. Biol.* **2**, a000695
30. Wu, H., Yin, Q.-F., Luo, Z., Yao, R.-W., Zheng, C.-C., Zhang, J., *et al.* (2016) Unusual processing generates SPA LncRNAs that sequester multiple RNA binding proteins. *Mol. Cell* **64**, 534–548
31. Thomas-Jinu, S., Gordon, P. M., Fielding, T., Taylor, R., Smith, B. N., Snowden, V., *et al.* (2017) Non-nuclear pool of splicing factor SFPQ regulates axonal transcripts required for normal motor development. *Neuron* **94**, 322–336.e5
32. Ha, K., Takeda, Y., and Dynan, W. S. (2011) Sequences in PSF/SFPQ mediate radioresistance and recruitment of PSF/SFPQ-containing complexes to DNA damage sites in human cells. *DNA Repair (Amst)* **10**, 252–259
33. Bottini, S., Hamouda-Tekaya, N., Mategot, R., Zaragosi, L.-E., Audebert, S., Pisano, S., *et al.* (2017) Post-transcriptional gene silencing mediated by microRNAs is controlled by nucleoplasmic Sfpq. *Nat. Commun.* **8**, 1189
34. Karczewski, K. J., Weisburd, B., Thomas, B., Solomonson, M., Ruderfer, D. M., Kavanagh, D., *et al.* (2017) The ExAC browser: displaying reference data information from over 60 000 exomes. *Nucl. Acids Res.* **45**, D840–D845
35. Schell, B., Legrand, P., and Fribourg, S. (2022) Crystal structure of SFPQ-NONO heterodimer. *Biochimie* **198**, 1–7
36. Strom, A. R., and Brangwynne, C. P. (2019) The liquid nucleome – phase transitions in the nucleus at a glance. *J. Cell Sci.* **132**, jcs235093
37. Guo, Y. E., Manteiga, J. C., Henninger, J. E., Sabari, B. R., Dall'Agnese, A., Hannett, N. M., *et al.* (2019) Pol II phosphorylation regulates a switch between transcriptional and splicing condensates. *Nature* **572**, 543–548
38. Schindelin, J., Arganda-Carreras, I., Frise, E., Kaynig, V., Longair, M., Pietzsch, T., *et al.* (2012) Fiji: an open-source platform for biological-image analysis. *Nature Methods* **9**, 676–682
39. McPhillips, T. M., McPhillips, S. E., Chiu, H.-J., Cohen, A. E., Deacon, A. M., Ellis, P. J., *et al.* (2002) Blu-ice and the distributed control system:

software for data acquisition and instrument control at macromolecular crystallography beamlines. *J. Synchrotron. Rad.* **9**, 401–406
40. Kabsch, W. (2010) Xds. *Acta Cryst. D* **66**, 125–132
41. Foadi, J., Aller, P., Alguel, Y., Cameron, A., Axford, D., Owen, R. L., *et al.* (2013) Clustering procedures for the optimal selection of data sets from multiple crystals in macromolecular crystallography. *Acta Cryst. D* **69**, 1617–1632
42. Evans, P. R., and Murshudov, G. N. (2013) How good are my data and what is the resolution? *Acta Cryst. D* **69**, 1204–1214
43. McCoy, A. J., Grosse-Kunstleve, R. W., Adams, P. D., Winn, M. D., Storoni, L. C., and Read, R. J. (2007) Phaser crystallographic software. *J. Appl. Crystallogr.* **40**, 658–674
44. Afonine, P. V., Grosse-Kunstleve, R. W., Echols, N., Headd, J. J., Moriarty, N. W., Mustyakimov, M., *et al.* (2012) Towards automated crystallographic structure refinement with phenix.refine. *Acta Cryst. D* **68**, 352–367
45. Emsley, P., Lohkamp, B., Scott, W. G., and Cowtan, K. (2010) Features and development of Coot. *Acta Cryst. D* **66**, 486–501